












RESEARCH ARTICLE | JUNE 12 2024

## Parallel on-chip micropipettes enabling quantitative multiplexed characterization of vesicle mechanics and cell aggregates rheology

Sylvain Landiech ; Marianne Elias; Pierre Lapèze ; Hajar Ajiyel ; Marine Plancke; Blanca González-Bermúdez ; Adrian Laborde; Fabien Mesnilgrente ; David Bourrier; Debora Berti ; Costanza Montis ; Laurent Mazonq; Jérémy Baldo; Clément Roux ; Morgan Delarue ; Pierre Joseph  



APL Bioeng. 8, 026122 (2024)

<https://doi.org/10.1063/5.0193333>



View  
Online



Export  
Citation



## APL Bioengineering

Special Topic:

## Bioengineering of the Brain

Guest Editors: Roberto Portillo Lara, Elena De Momi, Giuseppe Baselli

[Submit Today!](#)

# Parallel on-chip micropipettes enabling quantitative multiplexed characterization of vesicle mechanics and cell aggregates rheology



Cite as: APL Bioeng. 8, 026122 (2024); doi: 10.1063/5.0193333

Submitted: 21 December 2023 · Accepted: 24 May 2024 ·

Published Online: 12 June 2024



View Online



Export Citation



CrossMark

Sylvain Landiech,<sup>1</sup> Marianne Elias,<sup>1</sup> Pierre Lapèze,<sup>1</sup> Hajar Ajiyel,<sup>1</sup> Marine Plancke,<sup>1</sup> Blanca González-Bermúdez,<sup>2</sup> Adrian Laborde,<sup>1</sup> Fabien Mesnilgrete,<sup>1</sup> David Bourrier,<sup>1</sup> Debora Berti,<sup>3</sup> Costanza Montis,<sup>3</sup> Laurent Mazon,<sup>1</sup> Jérémy Baldo,<sup>1</sup> Clément Roux,<sup>4</sup> Morgan Delarue,<sup>1</sup> and Pierre Joseph<sup>1,a)</sup>

## AFFILIATIONS

<sup>1</sup>LAAS-CNRS, Université de Toulouse, CNRS, Toulouse, France

<sup>2</sup>Center for Biomedical Technology, Universidad Politécnica de Madrid, Pozuelo de Alarcón, Spain and Department of Materials Science, ETSI de Caminos, Canales y Puertos, Universidad Politécnica de Madrid, Madrid, Spain

<sup>3</sup>CSGI and Department of Chemistry, University of Florence, Sesto Fiorentino, Italy

<sup>4</sup>SoftMat, Université de Toulouse, CNRS, UPS, Toulouse, France

<sup>a)</sup> Author to whom correspondence should be addressed: [pierre.joseph@laas.fr](mailto:pierre.joseph@laas.fr)

## ABSTRACT

Micropipette aspiration (MPA) is one of the gold standards for quantifying biological samples' mechanical properties, which are crucial from the cell membrane scale to the multicellular tissue. However, relying on the manipulation of individual home-made glass pipettes, MPA suffers from low throughput and no automation. Here, we introduce the sliding insert micropipette aspiration method, which permits parallelization and automation, thanks to the insertion of tubular pipettes, obtained by photolithography, within microfluidic channels. We show its application both at the lipid bilayer level, by probing vesicles to measure membrane bending and stretching moduli, and at the tissue level by quantifying the viscoelasticity of 3D cell aggregates. This approach opens the way to high-throughput, quantitative mechanical testing of many types of biological samples, from vesicles and individual cells to cell aggregates and explants, under dynamic physico-chemical stimuli.

© 2024 Author(s). All article content, except where otherwise noted, is licensed under a Creative Commons Attribution-NonCommercial 4.0 International (CC BY-NC) license (<https://creativecommons.org/licenses/by-nc/4.0/>). <https://doi.org/10.1063/5.0193333>

## INTRODUCTION

Mechanics is ubiquitously at play in biology, from the level of cell membranes to the tissue scale. At the cell scale, response to stimuli is related to its cytoskeleton and nucleus but also strongly depends upon the deformability of its membrane.<sup>1</sup> At the multicellular scale, the capacity of cell assemblies to deform and flow is a determining factor in tissue homeostasis and evolution. This idea applies to developmental biology, since embryo morphogenesis is strongly intertwined with spatiotemporal changes and heterogeneity in fluidity.<sup>2,3</sup> It is also an essential ingredient for pathological situations such as solid cancers: the ability of cells to deform and spread, or jam, is key in disease progression.<sup>4</sup> Tissue rheology can thus be envisioned as a diagnostics tool,<sup>5</sup> or even to assist the prognosis of metastasis.<sup>6</sup>

Thus, strong efforts have been made in the last few decades to engineer quantitative tools assessing mechanical properties of cell

membranes,<sup>7</sup> cells,<sup>8</sup> and cell aggregates,<sup>9</sup> often relying on analogies with soft matter as proposed in Steinberg's pioneering work,<sup>10</sup> and on concepts of rheology.<sup>11</sup> One popular technique is micropipette aspiration (MPA),<sup>12–14</sup> both at the cell and tissue scale. MPA measures to what extent a vesicle, a cell, or a tissue enters a glass tube upon aspiration. It permits quantifying: bending and stretching rigidity for lipid vesicles mimicking cell membranes; apparent Young's modulus and effective viscosity for single cells;<sup>8</sup> and surface tension, elasticity, and viscosity for 3D cell aggregates.<sup>15</sup> MPA is one of the gold standards because it is quantitative, and it probes locally a zone that can be chosen. It also enables to some extent the change of solution surrounding the sample, and it can be coupled to other techniques like optical tweezers. However, it requires a complex dedicated setup: microscope, micromanipulator, and precise control of the pressure in the aspiration tube.<sup>15</sup> The control of the physico-chemical environment in real time

requires several micromanipulators, and the concentration of chemicals injected around the sample is non-homogeneous. Most importantly, MPA suffers from very low throughput ( $\sim 20$  tests/h for single cells,<sup>8</sup> a few tests/h for vesicles, and less than one test/h for cell aggregates<sup>15</sup>) since objects are intrinsically probed one by one, which can be limiting due to the high sample-to-sample variability that is often typical of biological systems.

Consequently, approaches to integrate micropipettes in microfluidic devices have been proposed in the very last few years. They target the above-mentioned limitations by designing channels enabling parallel trapping and fluid control at the cell (or cell aggregate) scale. A design relying on three-level fabrication was developed ten years ago by Lee *et al.* for cells,<sup>16</sup> which we improved in terms of alignment for the study of giant unilamellar vesicles (GUV).<sup>17</sup> Boot *et al.* recently adapted it to 3D cell aggregates.<sup>18</sup> While for this design microfluidics permits automation of objects injection, the rectangular geometry has intrinsic limitations: a quantitative analysis is complicated and some flow remains at the corner of the traps constituting the pipette, even though recent work described the different regimes of clogging rectangles with soft objects.<sup>19</sup> A two-level design was used to probe the viscoelasticity of cell nuclei in parallel thanks to constrictions,<sup>20</sup> simpler to implement than the previous one but still not fully quantitative. To relate the microscopic configuration to mechanical properties, 2D geometries permitting optical access combined with rheological measurements were used to characterize cell aggregate rearrangements<sup>21</sup> or vesicle prototissues,<sup>22</sup> but their extension to more realistic 3D tissues is far from obvious. Indeed, standard microfabrication techniques are planar, which limits the possibility of properly integrating circular traps. 3D printing technologies are associated with long writing time (several hours) for the resolution required here, and can hardly ensure nanometric surface roughness needed to properly aspirate vesicles or cell aggregates. As a way to eliminate the need for fluid confinement by surfaces, virtual walls microfluidics has recently been demonstrated to characterize both cell and spheroid mechanics,<sup>23</sup> with quite a high throughput but limited to a global probing of objects.

Thus, a micropipette aspiration method, quantitative but with a higher throughput than classical MPA, is still to be developed. We describe in this paper the SIMPA technology (sliding insert micropipette aspiration) addressing the above-mentioned requirements, both at the scales of vesicles and multicellular aggregates. It relies on the “sliding walls” proposed by Venzac *et al.*,<sup>24</sup> inserting sliding elements within PolyDimethylSiloxane (PDMS) chips. Here, rather than reconfigurability, which was the strong point raised in Ref. 24 and which, for instance, permitted studying confined tissue growth,<sup>25</sup> we specifically exploited the particular microfabrication features of the approach. Pipettes are designed and patterned by photolithography perpendicularly to the fabrication plane of the channel in which they are inserted (see Fig. 1). In this way, the objects injected in a microchannel can be blocked by pipettes of a chosen shape: a circular cross section permits quantitative measurements analyzed with classical models, since deformations occur like in standard MPA. Thanks to the integration, pipettes can be operated in parallel: we demonstrate it for 7 GUVs, and up to 23 spheroids. The throughput is thus multiplied by the number of pipettes in parallel when compared to classical MPA: with the SIMPA method, we achieve  $\sim 10$  tests/h for GUV and  $\sim 20$  tests/h for spheroids.

In the following, we explain in the methods the design principles and fabrication technique of the chips, as well as their fluidic operation.

We then demonstrate the interest of the technology by assessing two situations relevant to biophysics. First, we present the results obtained on vesicles: characterization of the elastic moduli of lipid bilayers with simple composition and study of the influence of sugar and cholesterol on these moduli. Second, we detail the use of the devices for 3D cellular aggregates: measurements of the surface tension and viscoelastic characteristics, and study of the influence of molecules targeting cell–cell adhesion.

## CONCLUSION

We present in this paper the SIMPA technology, a parallel, quantitative integrated aspiration micropipette method. We demonstrate its relevance to characterize quantitatively mechanics both at the cell membrane scale and at the multicellular scale. With respect to standard MPA, its throughput is multiplied by the number of pipettes in parallel, shown to be for this proof of concept 7 and 23 for GUVs and spheroids, respectively, leading to a throughput of order  $\sim 10$  tests/h for GUVs and  $\sim 20$  tests/h for spheroids. With respect to other integrated on-chip micropipettes,<sup>18,20,21</sup> our approach is the only one that combines circular geometry and parallel probing, in a user-friendly format. Thus, even if interesting analyses have recently been developed for squares or rectangles,<sup>19</sup> circular traps are quantitative by design, and they fully eliminate both anisotropy of the constraints and residual flows in the corners.

Several perspectives emerge from the versatility of the method, related to fluidic design. As the most obvious evolution, larger fluidic chambers, or pipettes placed at different z-positions, could lead to an even larger throughput by adding further parallel pipettes, if required. More interestingly, changing the chip design permits controlling physico-chemical stimuli around trapped objects.

As a further perspective, we could extend the single vesicle configuration to the probing of single cells, by using pipettes with diameters of order 2–5  $\mu\text{m}$ , which is fully compatible with photolithography techniques used in this work. By providing direct measurements of mechanical parameters, with a better throughput than conventional micropipettes, that could be very complementary to high throughput microfluidic deformability cytometry.<sup>50</sup>

Finally, specific versions of the technology can be developed to improve the quality of optics [thinner walls, see Fig. 4(c), or glass versions of the sliding elements, see [supplementary material](#) Video 6]. Overall, the SIMPA technology will help identify how collective properties emerge from individual cell deformations and rearrangements.

## METHODS

The microfluidic chips consisted of two parts, see Fig. 1(a). Here, we explain the main ingredients of its design, fabrication, and operation.

The first part is a PDMS chip, obtained by standard soft lithography. PDMS was cast and cured on a two-level mold patterned in a photosensitive dry film (SU-8), preferred to liquid photoresist since the thickness is as high as  $\sim 500 \mu\text{m}$ . After unmolding, holes were punched in PDMS for fluidic access.

The first level of the mold corresponds to the main fluidic channel, see Fig. 1(a). Its height is slightly superior to the maximum diameter of the objects to be probed with pipettes, typically  $\sim 100 \mu\text{m}$  for studies on vesicles and  $\sim 450 \mu\text{m}$  for spheroids.

The fluidic configuration is quite simple with one input and one output, the channel just getting wider at the location of sliding element insertion, to permit objects to be trapped in parallel. Note however that the design can be complexified for additional functions: we

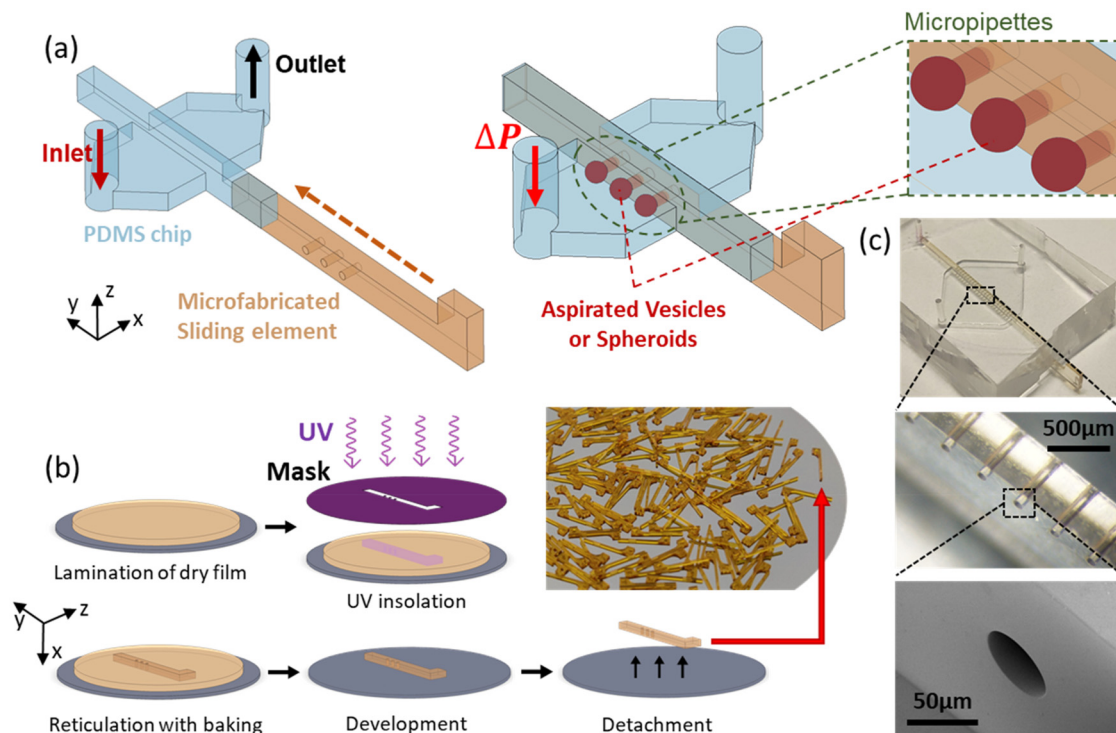


**FIG. 1.** Principle: On-chip pipettes integrated into a microfluidic chip thanks to sliding elements. (a) Parts view: PDMS chip and sliding element. Assembled view after insertion and schematic close-up of aspirated micro-objects (giant unilamellar vesicles or spheroids). (b) Microfabrication workflow of the sliding elements and photograph of dozens of them, manufactured in a single batch. (c) Micrographs and SEM close-ups of the pipettes integrated into the sliding elements.

demonstrate, for instance, injection of a chemical stimulus around spheroids, thanks to extra lateral channels (see Fig. SI-8).

The fluidic channel is intersected by another guide, integrated in the second layer of the mold, which is open to the outside. Its purpose is to accommodate the sliding element integrating the pipettes, the second part that composes our chips.

The PDMS part was then bonded by plasma on a thin layer of PDMS (50  $\mu\text{m}$ ), compromising between optical access for microscopy and deformation to avoid leakage.

The second element is the sliding element containing the pipettes to be integrated into the fluidic channel by insertion in the PDMS chip. This long parallelepiped including holes that constitute the pipettes was manufactured by photolithography using the same type of dry film, see Fig. 1(b). After optimizing fabrication parameters, we obtained pipettes with an aspect ratio up to 20 (25  $\mu\text{m}$  diameter for 500  $\mu\text{m}$  length) and with a low roughness: typically, only a few  $\sim 20$  nm-high asperities can be seen inside the pipette, as shown in Figs. 1(c) and SI-1. For pipettes with lower diameters [down to 12  $\mu\text{m}$  for GUVs, see Fig. 2(a), and 5  $\mu\text{m}$  for single cells], a multi-layer lamination protocol was used. Lamination was realized on a sacrificial layer (copper–titanium alloy), chemically etched after fabrication to release the sliding elements from the wafer. Since fabrication was realized by batches on a 4-in. wafer, up to 150 reusable SMPs (sliding micropipettes) could be obtained in a single fabrication run, which took a few hours.

Integration was made by inserting the SMP in the PDMS chip. This step could be achieved in a few minutes, either manually under a

binocular microscope, with alignment precision between the pipettes and the fluidic channel in the order of 50  $\mu\text{m}$ , or aided by a specific 3D-printed holder if better alignment was required (see Fig. SI-2). To reduce friction, an anti-adhesive coating (fluorinated silane deposited in the gas phase) was realized on the SMPs before insertion. Insertion was also facilitated thanks to isopropanol lubrication, eliminated afterward by evaporation (see the [supplementary material](#)).

Once inserted, the SMP blocked the fluid in the main channel by letting it flow only through its cylindrical holes. The height and width of the guide were 20% smaller than the height and width of the sliding element it received (typically 450  $\mu\text{m}$  for the guide and 550  $\mu\text{m}$  for the sliding element), which we found optimum for elastic deformation to ensure a good sealing upon insertion. We checked the absence of leakage in the whole range of the pressure controller (325 mbar). Thus, when a vesicle or a spheroid was injected into the inlet solution, it was carried by the flow until it arrived in front of one of the micropipettes into which it was blocked and aspirated. In the design of the SMPs, the center of the pipette was placed at a Z position permitting objects to be trapped without touching the bottom of the fluidic channel, while being in focus under the microscope.

Chip operation differed slightly for GUVs and spheroids and are detailed in the sections “micropipettes for vesicles”, and “micropipettes on cell aggregates”, respectively, and in the [supplementary material](#). Fluidic protocols shared some characteristics: after degassing and injection of the buffer to pre-wet the whole chip, the solution containing the objects of interest was injected to trap them at the pipettes.

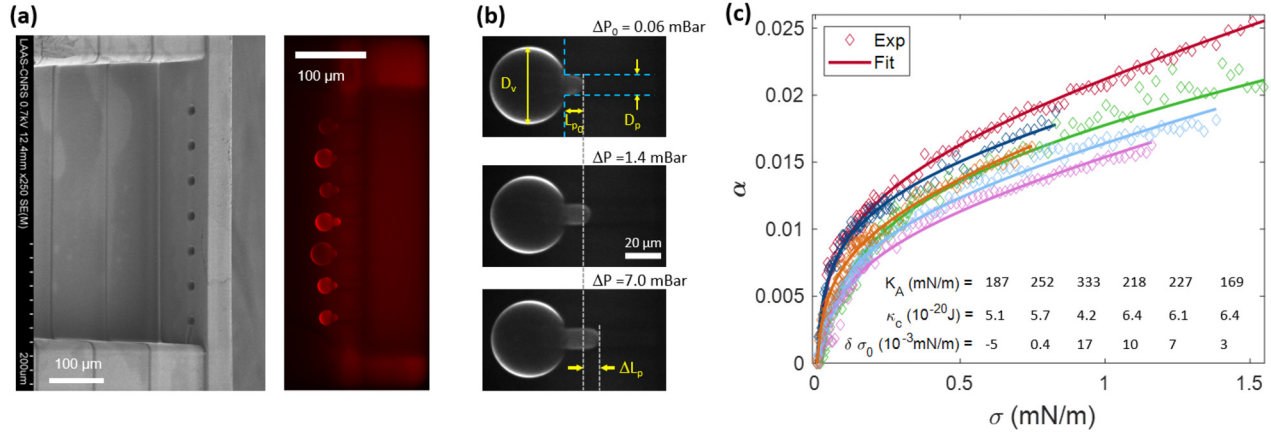


**FIG. 2.** On-chip pipettes applied to giant unilamellar vesicles to quantify the mechanics of lipid membranes (bending and stretching moduli). (a) SEM image of a sliding element with a design adapted to GUVs, including seven pipettes (12  $\mu\text{m}$  in diameter), and fluorescence microscopy micrograph of seven DOPC GUVs trapped within such pipettes inserted in a PDMS channel. (b) Fluorescence micrographs of a GUV blocked inside a 12- $\mu\text{m}$ -diameter pipette, for three values of the pressure difference applied to the vesicle. Reference situation  $\Delta P_0$  and two successive equilibrium positions. The quasistatic increase in pressure causes a progressive increase in the GUV area, quantified from the length of the GUV protrusion within the pipette. (c) Evolution of the relative area increase as a function of the tension for six DOPC GUVs of the same experimental run and fitted curve according to Eq. (1). The displayed numbers correspond to the outcomes of the fitting for this particular experiment, as a typical example of data dispersion.

Measurements of the mechanical properties were achieved by quantifying deformations (of the GUVs or spheroids) under a programmed pressure sequence, by optical microscopy and image analysis. Since the hydraulic resistance of the pipettes was much larger than those of the inlet and outlet channels, the pressure drop  $\Delta P$  applied to vesicles or spheroids was almost equal to the pressure drop applied on the whole channel  $\Delta P_{channel}$ , even in the case where some pipettes were not blocked.

This fabrication approach permitted the integration of cylindrical holes (or any extruded shape of arbitrary cross section) aligned with the main axis of fluidic channels, thanks to the photolithography of two elements along two orthogonal planes, which can hardly be achieved by standard manufacturing techniques. This feature makes SIMPA technology uniquely suited for high throughput micropipette aspiration, which we demonstrate in the following.

### MICROPIPETTES FOR VESICLES: ELASTIC MODULI OF LIPID MEMBRANES

The mechanics of a lipid bilayer can be described by two main parameters: its resistance to bending, quantified by the bending modulus  $\kappa_c$ , and its resistance to an increase in area per molecule (stretching modulus  $K_A$ ). These moduli determine how the area of a vesicle  $A$  increases with its tension  $\sigma$ , with reference to a state at low tension  $A_0$ ,  $\sigma_0$ . The relative area increase,  $\alpha = (A - A_0)/A_0$ , reads<sup>7,12</sup>

$$\alpha = \frac{k_B T}{8\pi\kappa_c} \ln(1 + \sigma/\sigma_0) + (\sigma - \sigma_0)/K_A, \quad (1)$$

where  $k_B$  is the Boltzmann constant, and  $T$  the temperature.

The increase in area at low tension is mostly controlled by the smoothing of thermal fluctuations against bending [first term of Eq. (1)], whereas for a higher tension (typically 1 mN/m), it is set by the stretching modulus  $K_A$  [second term of Eq. (1)].

In standard micropipette experiments, a progressively increasing tension is induced thanks to a pressure difference  $\Delta P$  applied to the

vesicle aspirated in the pipette. With the hypothesis that the pressure inside the vesicle is equilibrated, and that the tension is homogeneous, the vesicle tension can be deduced from the Laplace law according to

$$\sigma = \frac{\Delta P \cdot D_p}{4(1 - D_p/D_v)}, \quad (2)$$

where  $D_p$  and  $D_v$  are the pipette and vesicle diameters, respectively. With the additional hypothesis of constant vesicle volume during the experiment (low permeability of the lipid bilayer to solvent, few minutes experiments duration), and a first-order approximation ( $D_p^2 \Delta L_p \ll D_v^3$ ), the area increase is deduced from  $\Delta L_p$ , the position of the vesicle protrusion within the pipette with respect to the reference state ( $A_0$ ,  $\sigma_0$ ), see Fig. 2(b),

$$\Delta A = \pi D_p \Delta L_p \left(1 - \frac{D_p}{D_v}\right). \quad (3)$$

These principles apply to our microfluidic chips: we designed channels (100  $\mu\text{m}$  deep and 400  $\mu\text{m}$  wide), in which fluorescently labeled GUVs with a typical diameter of 50  $\mu\text{m}$ , obtained by standard electroformation (see the supplementary material), could flow. The channels integrated sliding elements with up to seven pipettes of diameter  $D_p \simeq 12 \mu\text{m}$ , see Fig. 2(a). The pressure was slowly increased by steps (3 s duration), to quantify the increase in  $L_p$  with  $\Delta P$ , see Fig. 2(b). The first step leading to a measurable GUV deformation was used as the reference state ( $\Delta P_0$ ,  $\Delta L_p = 0$ ,  $A_0$ ,  $\sigma_0$ ), see the top panel in Fig. 2(b).

For large enough GUVs ( $D_v \geq 2.5D_p$ ), standard image analysis was used to deduce  $\Delta L_p$  as a function of  $\Delta P$ . The relative area increase as a function of the tension was then calculated from Eqs. (2) and (3) for each GUV. The values of the bending and stretching moduli were then deduced by fitting Eq. (1) to the experimental curve. As exemplified in Fig. 2(c) showing six measurements realized in parallel, we have used a three-parameter fit, by letting the reference tension as a free parameter, in addition to the determination of  $\kappa_c$  and  $K_A$ . It was found

to reproduce more accurately the data trend in the bending regime than a two-parameter fit and fixed experimental reference tension  $\sigma_{0\text{exp}}$ . The associated difference between  $\sigma_{0\text{exp}}$  and the fitted value was in the range of  $\delta\sigma_0 \leq 10^{-5}$  mN/m, corresponding to a pressure difference  $\delta P \leq 3$  Pa. We independently characterized the accuracy of pressure control to be better than 0.5 Pa, so this value is a little higher than expected. We attribute this slight discrepancy to higher uncertainty in determining the absolute value of the pressure, even though relative variations are precisely measured. With this procedure, the curve superimposed on experimental data both for bending and stretching regime, with a coefficient of determination of the fitting  $R^2 \geq 0.99$ .

### Results for GUVs of simple composition and effects of sugar and cholesterol

The results obtained with GUVs of simple composition (bilayer of the mono-unsaturated lipids 1,2-dioleoyl-sn-glycero-3-phosphocholine, DOPC in sucrose solutions) are summarized in the histograms of Fig. 3(a). The statistics are slightly lower for the stretching modulus  $K_A$  ( $N=41$ ) than for the bending modulus  $\kappa_c$  ( $N=59$ ) because some GUVs escaped the pipettes at moderate pressure, without fully entering the stretching regime. We deduced the value of  $K_A$  only for vesicles escaping at a tension  $\sigma \geq 0.75$  mN/m. This fragility, which can be attributed to dispersion in the lysis tension, possibly due to minor defects in some GUVs, was not correlated with the measured value of  $K_A$  and  $\kappa_c$ .

We also investigated the effect of the sucrose concentration on the bilayer mechanics, for DOPC lipids, see Fig. 3(b). No systematic variation of both bending and stretching moduli was observed from 15 to 300 mM, within our experimental error.

Finally, we performed measurements on bilayers composed of DOPC mixed with up to 50% cholesterol, Fig. 3(c). We observed no dependence of the bending modulus on the cholesterol/lipid molar

fraction, whereas the stretching modulus almost doubled for molar fractions 0.4 and 0.5.

### Discussion: On-chip pipette to characterize vesicle mechanics

Overall, the results in Figs. 2 and 3 show that the proposed approach is suited to determine the mechanical properties of lipid membranes, similar to the classical micropipette aspiration. However, the throughput of our method is higher (roughly multiplied by the number of pipettes in parallel, 7 in Fig. 2) since several GUVs can be characterized in parallel. The integration in a microfluidic device has also the advantage of avoiding the manual search of vesicle and micro-manipulation of the pipette, since the driving flow in the channel naturally brings the vesicles to the pipettes, and facilitates the trapping of GUVs. In addition, pressure controllers used in routine microfluidic setups have sub-second response time and permit the automation of pressure vs time protocols.

The obtained values are reasonably consistent with the literature. For DOPC at room temperature, the determined stretching modulus  $K_A = 214 \pm 69$  mN/m falls within the range of most micropipette measurements (respectively,  $K_A = 210 \pm 25$  mN/m, 198 mN/m, and  $265 \pm 18$  mN/m for Refs. 26–28). The bending modulus we obtained ( $\kappa_c = 4.4 \pm 1.8 \times 10^{-20}$  J) is in the lower limit of published values for measurements with micropipettes (respectively,  $\kappa_c \sim 9.1 \pm 1.5 \times 10^{-20}$ ,  $8.5 \times 10^{-20}$ ,  $4.7 \times 10^{-20}$  J for DOPC in Refs. 26, 28, and 29) reported in a recent review<sup>30</sup> to be in the range of  $\kappa_c = 4\text{--}16 \times 10^{-20}$  J for monounsaturated lipids. It has to be mentioned that systematic differences between groups and measurement method are thoroughly discussed and only partly explained by differences in the probes scales or experimental protocols, in several reviews.<sup>7,30–32</sup>

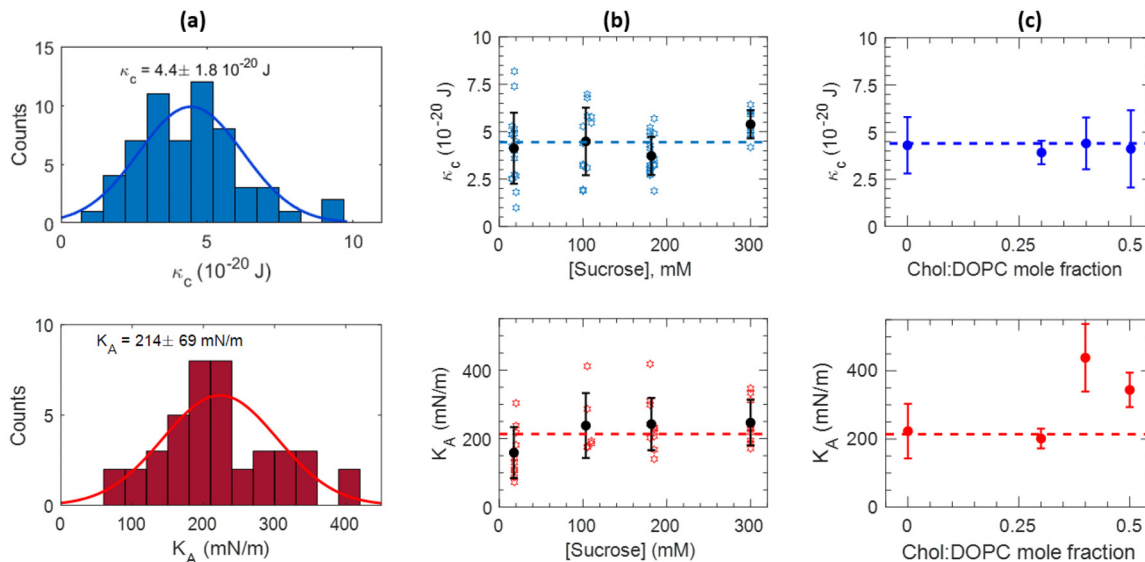


**FIG. 3.** Bending and stretching moduli of lipid bilayers. (a) Histograms of the bending (top) and stretching (bottom) moduli of DOPC membranes, and associated Gaussian fits. (b) Influence of the sucrose concentration on the value of the bending (top) and stretching (bottom) moduli, for DOPC membranes. (c) Influence of cholesterol on the bending (top) and stretching (bottom) moduli of mixed DOPC-cholesterol vesicles, as a function of the cholesterol/DOPC mole fraction.

The dispersion of our data is a bit higher than in the literature (coefficients of variation 41% and 29% for  $\kappa_c$  and  $K_A$ , respectively). GUVs synthesized via electroformation have inherent variability. We also attribute the dispersion to the fact that the only eliminated GUVs were those with diameter  $D_v \leq 2.5D_p$ , or with visible defects (such as internal vesicles), contrary to standard micropipette aspiration where the operator arbitrarily chooses the GUV to be probed.

The absence of influence of sugar concentration we observed [Fig. 3(b)] is consistent with most recent observations and discussion of the literature, even though this is still a quite controversial issue.<sup>32–35</sup>

When varying the membrane composition by mixing DOPC with cholesterol, we observed no change in the bending modulus, from pure DOPC up to the maximum cholesterol content tested (0.5 mol/mol). On the opposite, a twofold increase was observed for  $K_A$  for increasing cholesterol content, with a possible threshold between 0.3 and 0.4 molar fraction in cholesterol. These observations complete a rich literature on the issue of cholesterol's influence on membrane structure and properties. Bending rigidity was shown to be strongly lipid dependent,<sup>36,37</sup> stiffening by cholesterol being observed only for saturated lipids, with no effect for mono-unsaturated lipids, such as the DOPC, used in the present study,<sup>38,39</sup> or even slight softening related to coupling between bending and cholesterol localization.<sup>40</sup>

Finally, changing the chip design permits controlling physico-chemical stimuli around trapped objects. Pipettes including slits to let a fraction of the flow pass can be used to probe vesicles while submitted to shear stress: by using cross-shaped pipettes, we have observed that shear stress affects lipid domains, as demonstrated in Ref. 41, see Fig. SI-7. Since a microfluidic lateral channel can be integrated into the design, the approach is well suited for temporal change of the chemical environment surrounding the GUVs. It opens interesting perspectives

to investigate, for example, the kinetics of the interaction of lipid bilayers with biomolecules or relevant synthetic entities (molecules, macromolecules, or nanosystems).

### MICROPIPETTES ON CELL AGGREGATES: QUANTIFYING SPHEROIDS' RHEOLOGY

Many biological tissues behave as viscoelastic fluids, which is both due to the properties of individual cells (cytoskeleton and nucleus), and to the way they assemble in the tissue (extracellular matrix and adhesion between cells). Thus, when a spheroid (simple 3D cell aggregate) is probed by micropipette aspiration with a pressure step, it reacts with two different regimes. First, an instantaneous deformation is observed, directly linked to the tissue's elastic properties. Then, over time, the tissue flows into the micropipette like a viscous fluid. Several viscoelastic models describe this type of material, but the modified Kelvin–Voigt shown in the insert of Fig. 4(b) is the simplest that closely reproduces the response observed in Fig. 4(b). It consists of a Kelvin–Voigt element (spring  $k_1$  in parallel with damper  $\mu_c$ ), modified by the spring  $k_2$  to account for an instantaneous elastic response, in series with a dashpot  $\mu_t$ , which corresponds to long-term viscous flow. In this description of the tissue as a soft material, viscosity and elasticity are completed by the aggregate's surface tension  $\gamma$ , excess of surface energy that originates from a combination of the interaction between cells, and differences in cortical tension between the peripheric and the core cells.<sup>10,42</sup> In a standard micropipette experiment, a spheroid of radius  $R$  is aspirated in a pipette of radius  $R_p$  with a suction pressure  $\Delta P$ . The effective force inducing spheroid deformation reads  $f = \pi R_p^2(\Delta P - \Delta P_c)$ , where  $\Delta P_c = 2\gamma(\frac{1}{R_p} - \frac{1}{R})$  is the Laplace pressure generated by the curvature imposed by the pipette.  $\Delta P_c$  corresponds to the minimum pressure needed for the spheroid to continuously flow

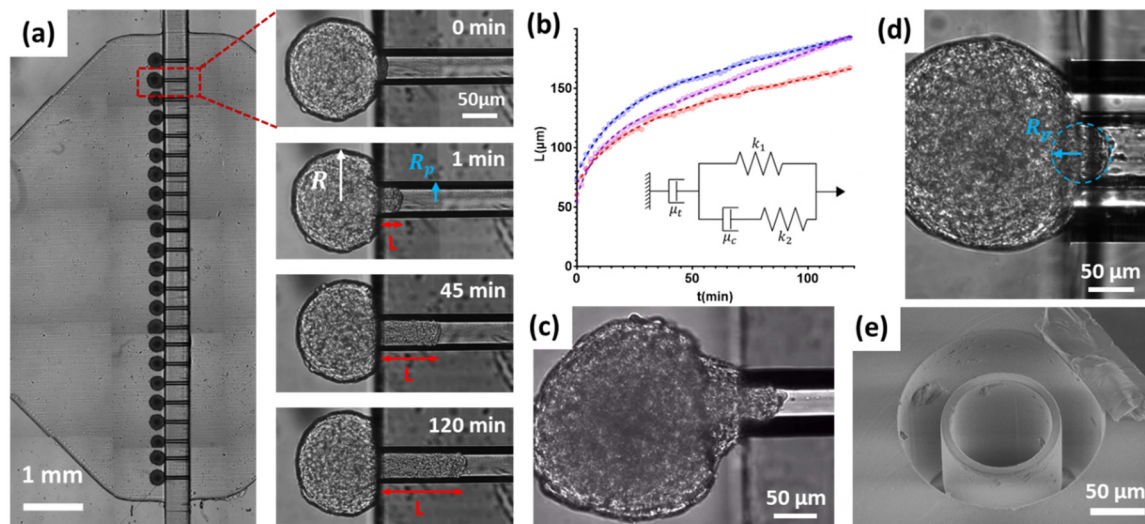


**FIG. 4.** On-chip pipettes applied to 3D cellular aggregates to quantify their viscosity and elasticity. (a) Micrograph of 23 spheroids trapped in the pipettes in the SIMPA chip. Close-up on a single micropipette: time-lapse of the aspiration of one A338 spheroid submitted to a pressure step  $\Delta P = 50$  mbar from  $t = 0$  s. (b) Evolution of the spheroids' positions  $L(t)$  in the pipette as a function of time for three simultaneous parallel measurements, and fitted curves according to Eq. (4). (c) Micrograph of a spheroid just after release of the aspiration pressure. The conical shape indicates that Laplace pressure is not the only process expelling the spheroid from the pipette, during retraction. (d) Micrograph of a spheroid aspirated with a pressure just equal to the Laplace pressure  $\Delta P_c$ , leading to a radius equal to the pipette's radius. (e) SEM image of the pipette design with a thin wall, used to improve the optical quality of the image in (d).

inside the pipette. For  $\Delta P > \Delta P_c$ , the spheroid's response to a differential pressure step can be written, in terms of its temporal elongation  $L(t)$  inside the pipette [see Fig. 4(a)], as

$$L(t) = \frac{f}{k_1} \left( 1 - \frac{k_2}{k_1 + k_2} e^{-\frac{t}{\tau_c}} \right) + \frac{f}{\mu_t} t, \quad (4)$$

where  $\tau_c = \frac{\mu_c(k_1 + k_2)}{k_1 k_2}$  is a viscoelastic characteristic time.

The first term in Eq. (4) refers to a viscoelastic solid, with two elastic moduli acting at two timescales: a first modulus  $E_i = (k_1 + k_2)/\pi R_p$ , associated with an instantaneous deformation of the spheroid, and a second elastic modulus  $E = k_1/\pi R_p$ , which comes into play after a typical time  $\tau_c$ . These two elastic moduli are usually attributed to the cellular cytoskeleton's reaction to pressure: the elasticity of the actin cortex is first assessed and fibers then rearrange, leading to a softer long-time elastic response.

The second term describes flow at the tissue level, and it corresponds to the constant speed flow of a fluid of viscosity  $\eta = \mu_t/3\pi^2 R_p$  inside the pipette, with the hypothesis that viscous dissipation occurs only at the inlet, due to cell rearrangements. As detailed in Ref. 14, this regime neglects wall friction, which is achieved thanks to surface treatment limiting cell adhesion on the pipette's walls.

It is worth noting that these quantitative relationships between the Kelvin–Voigt parameters ( $k_1$ ,  $k_2$ ,  $\mu_t$ ) and the macroscopic viscoelastic moduli ( $E_i$ ,  $E$ ,  $\eta$ ) slightly depend on the thickness of the pipette wall. They are correct for our SIMPA configuration (thick walls), whereas they need to be corrected by a few percent for classical MPA (thin walls), as discussed in Refs. 43 and 44 regarding elasticity and viscosity, respectively.

We have developed microfluidic chips enabling parallel aspiration of up to 23 spheroids, see Fig. 4(a). The channel height was 450  $\mu\text{m}$  to accommodate all spheroid sizes. The chamber width was 10 mm for the 23-position chip (2 mm for the 5-position chip). A single microfabrication run allowed us to manufacture around 150 SMPs, see photograph in Fig. 1(b), which permitted us to test different pipette diameters and designs. Most experiments were conducted with 70  $\mu\text{m}$  diameter pipettes, chosen as a compromise: much smaller than spheroids size, and significantly larger than cells size, for the granular nature of the tissue not to be too critical for the continuous description of the rheological model. Pipettes were 500  $\mu\text{m}$  in length. A pressure step was applied to the spheroids, as detailed in the supplementary material. As mentioned in the Methods, the total channel pressure drop would be exerted on the pipettes even without spheroids blocking all of them, because they dominate the chip's hydraulic resistance. However, we only conducted experiments in which one spheroid is present in each pipette, to avoid the flow of buffer in free pipettes, that could affect the overall pressure difference because of a hydrostatic contribution upon increase in the outlet reservoir level.

To validate quantitatively the SIMPA approach with respect to MPA, we performed measurements on the murine sarcoma cell line S180-GFP that was characterized by Guevorkian *et al.*<sup>13</sup> by MPA. Since Laplace pressure contributes to the spheroid's flow [see Eq. (4)], the surface tension  $\gamma$  needs to be determined to deduce the viscoelastic parameters. Like in Ref. 13, aspiration was followed by retraction experiments, in which Laplace pressure is the only source of movement. The histograms of measured viscoelastic parameters are plotted in Fig. SI-4 ( $N = 23$ ). We obtained  $\gamma = 10.8 \pm 2.4$  mN/m,  $\eta = 1.37 \pm 0.03 \times 10^5$  Pa s,  $E = 213 \pm 17$  Pa, and  $E_i = 773 \pm 47$  Pa. The values of the

viscosity and long-time elasticity are fully consistent with the results reported in Ref. 13 ( $\eta = 1.9 \pm 0.3 \times 10^5$  Pa s, elastic modulus deduced from an average of relaxation times:  $E = 700 \pm 100$  Pa), given that the cell line may have slightly evolved since 2010, and more importantly that the culture conditions to form the spheroids were not exactly the same in the two studies.

For A338 mouse pancreatic cancer cell spheroids, a typical time-lapse for one position is shown on the right panel of Fig. 4(a), and in supplementary material Video 1. The position of the spheroid protrusion as a function of time  $L(t)$  was determined by a custom image segmentation algorithm described in the supplementary material, see Fig. SI-5 and supplementary material Video 3. Typical results of a single experiment driven on A338 spheroids are displayed in Fig. 4(b), together with the fit of these results by Eq. (4).

However, regarding surface tension, we observed for this cell line a complex conical shape of the spheroid upon retraction, see Fig. 4(c) and supplementary material Video 2, and its fast ejection from the pipette. Several mechanisms could explain this behavior: stored elastic energy could contribute to expelling the spheroid out of the pipette (similarly to what is mentioned in Ref. 18), and additionally thanks to low wall friction the spheroid could slide upstream without dissipation and progressively round up at the pipette's corner because of surface tension. We thus used alternatives to such retraction experiments and measured  $\gamma$  by directly characterizing Laplace pressure thanks to other sets of experiments. We quantified the minimum critical pressure leading to continuous flow of the spheroid  $\Delta P_{crit}$ , which should also correspond to the pressure for which the radius of the spheroid meniscus (formed by cells at its surface within the pipette) equals the pipette radius, see Fig. 4(d). This set of experiments was realized on a specially designed thin-wall pipette, see Fig. 4(e), to improve the quality of optics. Both pressures were determined to be very close and equal to  $\Delta P_{c-crit} = 5 \pm 0.5$  mbar. These measurements led to a value of the surface tension  $\gamma_{crit} = 10 \pm 1$  mN/m. We also quantified the ratio  $\gamma/\eta$  from the dynamics of spheroid fusion,<sup>45</sup> see the supplementary material, Fig. SI-6. These independent off-chip experiments led to  $\gamma_{fusion} = 4.5 \pm 0.9$  mN/m. The fusion experiment mainly probes the external layers of the spheroid, and the surface tension of cell aggregates was recently discussed theoretically to be a multi-scale complex concept,<sup>46</sup> so that different configurations could lead to slightly different results. The viscosity retained for this fitting was the one deduced from aspiration experiments. In addition, note that in both cases, the value corresponds to the surface tension at low stress, referred to as  $\gamma_0$  in previous studies, which have evidenced a possible increase in  $\gamma$  upon aspiration.<sup>13</sup> We finally retained the on-chip measured value  $\gamma_{crit}$ , since it was determined in the same flow configuration as the pipette aspiration. It is in the typical range of literature measurement of biological tissues' surface tension,<sup>47</sup> even though most available data are on less cohesive configurations than the epithelial one probed here. Let us mention that since the applied pressure in aspiration experiments was significantly higher than the typical Laplace pressure, an error in surface tension determination would not critically affect the determination of viscoelastic parameters.

With this value of the surface tension, we extracted the rheological parameters from the fitting of the experimental curves  $L(t)$  with Eq. (4), see Fig. 4(b). The fittings closely reproduced the trends of the experiments. Graphically, tissue viscosity is deduced from the slope at a long time, whereas the first (short-time) elastic modulus  $E_i$  can be



deduced from the initial instantaneous elongation of the spheroid, the second modulus  $E$  from the intercept of the long-time linear flow regime with the vertical axis, and  $\tau_c$  from the typical timescale to reach this regime.

### Measuring viscoelastic properties of spheroids: Results and discussion

The results obtained with A338 spheroids are shown in Fig. 5(a). All ( $N = 134$ ) measurements were realized with the 5-pipettes design, in about 30 experiments, each lasting a few hours, which demonstrates the high throughput of the method. We measured elastic moduli  $E = 1.4 \pm 0.5$  kPa,  $E_i = 2.5 \pm 0.9$  kPa, and a timescale  $\tau_c = 15.3 \pm 8.1$  min (error bars indicates the standard deviation). For viscosity, the distribution was observed to be better fitted by a lognormal distribution than by a Gaussian. The maximum (mode) of the fitted distribution was  $\eta_{ln} = 1.20$  MPa.s, with a distribution width  $\sigma_{\eta-ln} = 0.67$  MPa.s. We observed a more reduced dispersion between spheroids of the same batch: the average of standard deviations deduced from single experiments (5 or 23 simultaneous measurements) was  $\sigma_{\eta-batch} = 0.5$  MPa.s and  $\sigma_{E_i-batch} = 0.35$  kPa for the viscosity and short-time elasticity  $E_i$ , respectively. These values can be interpreted as an upper bound of the measurement uncertainty, demonstrating the reproducibility of the technique. The width of the histograms in Fig. 5(a) mostly originates from biological variability.

To the best of our knowledge, no viscoelastic measurements have been published for this cell line. However, the high value of viscosity and elasticity, about ten times the typical values measured for very

dynamic embryonic tissues,<sup>48</sup> is consistent with the strong cohesion of pancreatic epithelial-like tissues.

We also assessed the effect of ethylenediaminetetraacetic acid (EDTA). EDTA affects adhesion between cells by chelating metallic ions, including calcium, necessary for adhesion proteins to operate. We incubated the cells with EDTA during the formation of the spheroids before measuring viscoelastic properties. The results are shown in Figs. 5(e) and 5(f). The viscosity was significantly reduced for spheroids incubated with EDTA with respect to the control, whereas short-time elasticity was not affected. This behavior is consistent with a reduced adhesion facilitating rearrangement of cells (T4 events<sup>21</sup>), leading to decreased viscosity, whereas elasticity, originating mostly from cells' cytoskeletons, was not strongly impacted.

We now discuss the specificities of the SIMPA technology for spheroid rheology, with respect to existing methods.

First, the approach benefits from the advantages of standard MPA: it is quantitative, and it probes optically determined locations of an object, which opens the possibility to test different zones of a tissue for non-spherical aggregate. MPA applies forces from the external cell layers, which can give complementary information to methods applying homogeneous stress, like magnetic rheometry.<sup>49</sup> In our chips, since it is the microfluidic flow that pushes the spheroids toward the pipettes, the spheroid's orientation and the precise point they contact the pipette's inlet cannot be controlled by the operator independently of the fluidic design, which can appear as a limitation. However, for non-spherical objects, it could turn into an advantage: the shape of the upstream channel and the location of pipettes on the sliding element could be specifically designed to set this orientation and probe well-defined areas.

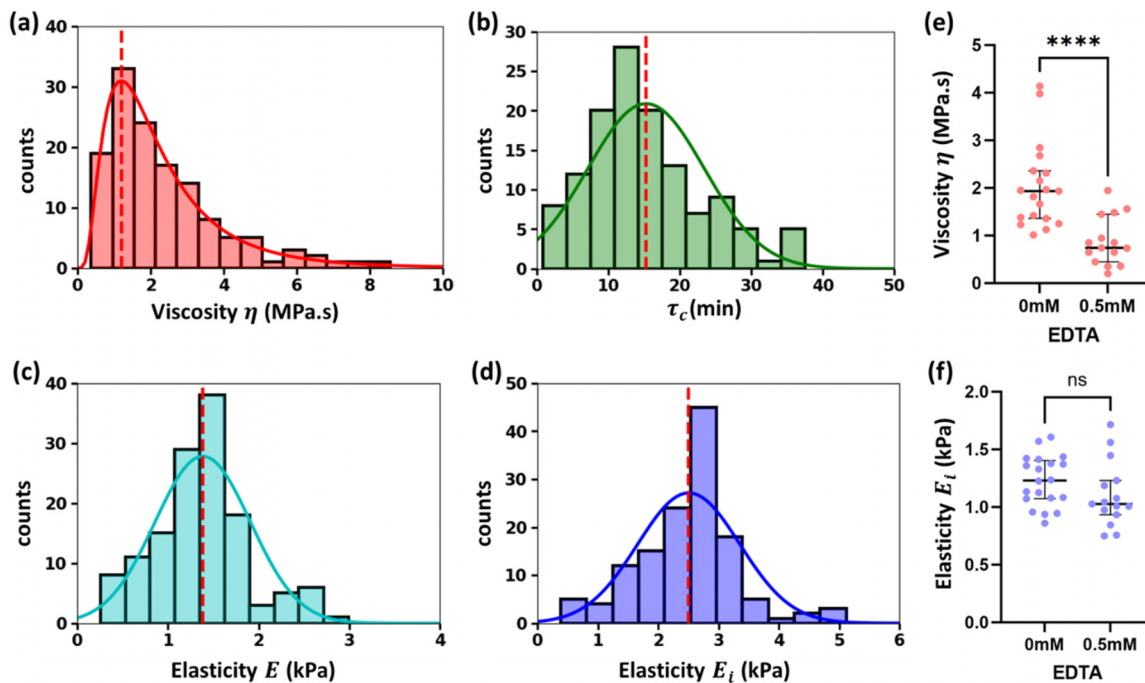


**FIG. 5.** Viscoelastic properties of A338 cellular aggregates: histograms of the viscosity (a), characteristic viscoelastic time (b), long-time elasticity (c), and short-time elasticity (d). (e) and (f) Influence of EDTA on the spheroids' viscosity and short-time elasticity.

The SIMPA technology has unique features compared to standard MPA: the throughput is multiplied by the number of spheroids that can be probed in parallel (demonstrated to be up to 23 in this article). In addition, the chip format permits the use of low volumes of sample (typically a few hundred microliters), with a spontaneous spheroid loading since the flow naturally pushes the spheroids to the free SMPs. The chips can also be washed and reused, and the spheroids extracted out of the chip for further characterization. It is possible to keep spheroids for long times (we observed spheroids stable for three days with no visible necrosis). This comes from the environmental chamber surrounding the chip on the microscope (temperature set to 37 °C and 5% CO<sub>2</sub>), but also from PDMS permeability to oxygen, and from a fast diffusion of nutrients within the chips. Finally, adding lateral fluidic channels close to the sliding element permits changing in real time the chemical environment of trapped spheroids, see Fig. SI-8. As a proof of concept, we demonstrated the dynamic exposure of trapped spheroids to microparticles, see [supplementary material Videos 4 and 5](#). This type of design could be relevant to study the response to drugs at short timescales, typically seconds or minutes. Quantifying the influence of different drugs, at different timescales, should improve our understanding of the microscopic origin of tissue rheology. In the same perspective, the technology can apply a dynamic pressure stimulus, as in Ref. 49, which is a relevant way to assess the validity of different rheological models, or to apply spatiotemporal stimulations such as the ones originating from heart beating or circadian cycle.

## SUPPLEMENTARY MATERIAL

See the [supplementary material](#) for microfabrication protocols, preparation of GUVs, cell culture and preparation of spheroids, and microfluidic protocols; SEM images of the pipettes (Fig. SI-1); as well as the device to control the insertion of the pipettes (Fig. SI-2); characterization of the dry film fluorescence (Fig. SI-3); full histograms of the viscoelastic properties (Fig. SI-4); image analysis algorithm (Fig. SI-5); the independent off-chip measurement of surface tension (Fig. SI-6); an alternative geometry enabling to expose trapped object to a fluid shear stress (Fig. SI-7), together with its use to demonstrate the effect of shear on lipid domains; a second alternative geometry to control the chemical microenvironment around trapped objects (Fig. SI-8); and finally, six supplementary videos are included, to exemplify the different steps and possibilities of the pipettes, whose legends are provided at the end of the [supplementary material](#) text.

## ACKNOWLEDGMENTS

This work was supported in part by CNRS through the PICS CNRS program “Microfluidics for Soft Matter,” and by INSIS-CNRS. This work was partly supported by LAAS-CNRS micro and nanotechnologies platform member of the French RENATECH network. BGB was supported by a fellowship from the “Programa Propio de I + D + I 2022” of Universidad Politécnica de Madrid. Funding by “ADI, Université de Toulouse, Région Occitanie,” and by Federation Fermat, Université de Toulouse, is acknowledged. We thank Benjamin Reig for SEM imaging, Sandrine Souleille for microfluidics experiments, Charline Blatché for cell culture, and Julien Roul for help in microscopy experiments. We thank Karine Guevorkian and Gregory Beaune for gently providing the S180 cell line.

## AUTHOR DECLARATIONS

### Conflict of Interest

The authors have no conflicts to disclose.

### Ethics Approval

Ethics approval is not required.

### Author Contributions

Sylvain Landiech and Marianne Elias contributed equally to this work.

**Sylvain Landiech:** Data curation (lead); Formal analysis (equal); Investigation (equal); Writing – review & editing (equal). **Debora Berti:** Supervision (supporting). **Costanza Montis:** Supervision (supporting). **Laurent Mazenq:** Investigation (supporting). **Jérémy Baldo:** Investigation (supporting). **Clément Roux:** Conceptualization (equal); Funding acquisition (equal); Supervision (equal); Writing – review & editing (equal). **Morgan Delarue:** Conceptualization (equal); Formal analysis (equal); Supervision (supporting); Writing – review & editing (supporting). **Pierre Joseph:** Conceptualization (lead); Formal analysis (lead); Funding acquisition (lead); Supervision (equal); Writing – original draft (equal); Writing – review & editing (lead). **Marianne Elias:** Data curation (equal); Formal analysis (equal); Investigation (equal); Writing – review & editing (supporting). **Pierre Lapèze:** Data curation (supporting); Investigation (supporting); Writing – review & editing (supporting). **Hajar Ajiyel:** Data curation (supporting); Investigation (supporting). **Marine Plancke:** Investigation (supporting). **Blanca González-Bermúdez:** Investigation (supporting). **Adrian Laborde:** Investigation (supporting); Methodology (supporting). **Fabien Mesnilgrete:** Investigation (supporting). **David Bourrier:** Investigation (supporting); Methodology (supporting).

## DATA AVAILABILITY

The data that support the findings of this study are available from the corresponding author upon reasonable request.

## REFERENCES

- <sup>1</sup>A. Diz-Muñoz, O. D. Weiner, and D. A. Fletcher, “In pursuit of the mechanics that shape cell surfaces,” *Nat. Phys.* **14**, 648–652 (2018).
- <sup>2</sup>N. I. Petridou and C.-P. Heisenberg, “Tissue rheology in embryonic organization,” *EMBO J.* **38**, e102497 (2019).
- <sup>3</sup>P.-F. Lenne and V. Trivedi, “Sculpting tissues by phase transitions,” *Nat. Commun.* **13**, 664 (2022).
- <sup>4</sup>L. Oswald, S. Grosser, D. M. Smith, and J. A. Käs, “Jamming transitions in cancer,” *J. Phys. Appl. Phys.* **50**, 483001 (2017).
- <sup>5</sup>P. Deptula *et al.*, “Tissue rheology as a possible complementary procedure to advance histological diagnosis of colon cancer,” *ACS Biomater. Sci. Eng.* **6**, 5620–5631 (2020).
- <sup>6</sup>P. Gottheil *et al.*, “State of cell unjamming correlates with distant metastasis in cancer patients,” *Phys. Rev. X* **13**, 031003 (2023).
- <sup>7</sup>P. Bassereau, B. Sorre, and A. Lévy, “Bending lipid membranes: Experiments after W. Helfrich’s model,” *Adv. Colloid Interface Sci.* **208**, 47–57 (2014).
- <sup>8</sup>B. González-Bermúdez, G. V. Guinea, and G. R. Plaza, “Advances in micropipette aspiration: Applications in cell biomechanics, models, and extended studies,” *Biophys. J.* **116**, 587–594 (2019).
- <sup>9</sup>D. Gonzalez-Rodriguez, K. Guevorkian, S. Douezan, and F. Brochard-Wyart, “Soft matter models of developing tissues and tumors,” *Science* **338**, 910–917 (2012).

- <sup>10</sup>M. S. Steinberg, "Reconstruction of tissues by dissociated cells," *Science* **141**, 401–408 (1963).
- <sup>11</sup>R. Chotard-Ghodsna and C. Verdier, "Rheology of living materials," in *Modeling of Biological Materials*, edited by F. Mollica, L. Preziosi, and K. R. Rajagopal (Birkhäuser, Boston, MA, 2007).
- <sup>12</sup>E. Evans and W. Rawicz, "Entropy-driven tension and bending elasticity in condensed-fluid membranes," *Phys. Rev. Lett.* **64**, 2094–2097 (1990).
- <sup>13</sup>K. Guevorkian, M.-J. Colbert, M. Durth, S. Dufour, and F. Brochard-Wyart, "Aspiration of biological viscoelastic drops," *Phys. Rev. Lett.* **104**, 218101 (2010).
- <sup>14</sup>K. Guevorkian, F. Brochard-Wyart, and D. Gonzalez-Rodriguez, "Flow dynamics of 3D multicellular systems into capillaries," in *Viscoelasticity and Collective Cell Migration*, edited by I. Pajic-Lijakovic and E. H. Barriga (Academic Press, 2021), Chap. 8, pp. 193–223.
- <sup>15</sup>K. Guevorkian and J.-L. Maître, "Micropipette aspiration," in *Methods in Cell Biology* (Elsevier, 2017), Vol. 139, pp. 187–201.
- <sup>16</sup>L. M. Lee and A. P. Liu, "A microfluidic pipette array for mechanophenotyping of cancer cells and mechanical gating of mechanosensitive channels," *Lab Chip* **15**, 264–273 (2014).
- <sup>17</sup>M. Elias *et al.*, "Microfluidic characterization of biomimetic membrane mechanics with an on-chip micropipette," *Micro Nano Eng.* **8**, 100064 (2020).
- <sup>18</sup>R. C. Boot *et al.*, "High-throughput mechanophenotyping of multicellular spheroids using a microfluidic micropipette aspiration chip," *Lab Chip* **23**, 1768–1778 (2023).
- <sup>19</sup>C. P. Moore, J. Husson, A. Boudaoud, G. Amselem, and C. N. Baroud, "Clogging of a rectangular slit by a spherical soft particle," *Phys. Rev. Lett.* **130**, 064001 (2023).
- <sup>20</sup>P. M. Davidson *et al.*, "High-throughput microfluidic micropipette aspiration device to probe time-scale dependent nuclear mechanics in intact cells," *Lab Chip* **19**, 3652–3663 (2019).
- <sup>21</sup>S. L. Thili, F. Graner, and H. Delanoë-Ayari, "A microfluidic platform to investigate the role of mechanical constraints on tissue reorganization," *Development* **149**, dev200774 (2022).
- <sup>22</sup>M. Layachi, L. Casas-Ferrer, G. Massiera, and L. Casanellas, "Rheology of vesicle prototissues: A microfluidic approach," *Front. Phys.* **10**, 1045502 (2022).
- <sup>23</sup>M. H. Panhwar *et al.*, "High-throughput cell and spheroid mechanics in virtual fluidic channels," *Nat. Commun.* **11**, 2190 (2020).
- <sup>24</sup>B. Venzac *et al.*, "Sliding walls: A new paradigm for fluidic actuation and protocol implementation in microfluidics," *Microsyst. Nanoeng.* **6**, 18 (2020).
- <sup>25</sup>Z. B. Meriem *et al.*, "A microfluidic mechano-chemostat for tissues and organisms reveals that confined growth is accompanied with increased macromolecular crowding," *Lab. Chip* **23**, 4445–4455 (2023).
- <sup>26</sup>L. Lu, W. J. Doak, J. W. Schertzer, and P. R. Chiarot, "Membrane mechanical properties of synthetic asymmetric phospholipid vesicles," *Soft Matter* **12**, 7521–7528 (2016).
- <sup>27</sup>D. Chen and M. M. Santore, "Hybrid copolymer–phospholipid vesicles: Phase separation resembling mixed phospholipid lamellae, but with mechanical stability and control," *Soft Matter* **11**, 2617–2626 (2015).
- <sup>28</sup>W. Rawicz, K. C. Olbrich, T. McIntosh, D. Needham, and E. Evans, "Effect of chain length and unsaturation on elasticity of lipid bilayers," *Biophys. J.* **79**, 328–339 (2000).
- <sup>29</sup>P. Shchelokovskyy, S. Tristram-Nagle, and R. Dimova, "Effect of the HIV-1 fusion peptide on the mechanical properties and leaflet coupling of lipid bilayers," *New J. Phys.* **13**, 025004 (2011).
- <sup>30</sup>D. Boichchio and L. Monticelli, "The membrane bending modulus in experiments and simulations: A puzzling picture," in *Advances in Biomembranes and Lipid Self-Assembly*, edited by A. Iglič, C. V. Kulkarni, and M. Rappolt (Academic Press, 2016), Vol. 23, Chap. 5, pp. 117–143.
- <sup>31</sup>J. F. Nagle, "Introductory Lecture: Basic quantities in model biomembranes," *Faraday Discuss.* **161**, 11–29 (2013).
- <sup>32</sup>J. F. Nagle, M. S. Jablin, S. Tristram-Nagle, and K. Akabori, "What are the true values of the bending modulus of simple lipid bilayers?," *Chem. Phys. Lipids* **185**, 3–10 (2015).
- <sup>33</sup>V. Vitkova, J. Genova, M. D. Mitov, and I. Bivas, "Sugars in the aqueous phase change the mechanical properties of lipid mono- and bilayers," *Mol. Cryst. Liq. Cryst.* **449**, 95–106 (2006).
- <sup>34</sup>J. F. Nagle, M. S. Jablin, and S. Tristram-Nagle, "Sugar does not affect the bending and tilt moduli of simple lipid bilayers," *Chem. Phys. Lipids* **196**, 76–80 (2016).
- <sup>35</sup>R. Dimova, "Recent developments in the field of bending rigidity measurements on membranes," *Adv. Colloid Interface Sci.* **208**, 225–234 (2014).
- <sup>36</sup>R. S. Gracià, N. Bezlyepkina, R. L. Knorr, R. Lipowsky, and R. Dimova, "Effect of cholesterol on the rigidity of saturated and unsaturated membranes: Fluctuation and electrodeformation analysis of giant vesicles," *Soft Matter* **6**, 1472 (2010).
- <sup>37</sup>J. Eid, H. Razmazma, A. Jraij, A. Ebrahimi, and L. Monticelli, "On calculating the bending modulus of lipid bilayer membranes from buckling simulations," *J. Phys. Chem. B* **124**, 6299–6311 (2020).
- <sup>38</sup>J. F. Nagle *et al.*, "A needless but interesting controversy," *Proc. Natl. Acad. Sci.* **118**, e2025011118 (2021).
- <sup>39</sup>J. Pan, S. Tristram-Nagle, and J. F. Nagle, "Effect of cholesterol on structural and mechanical properties of membranes depends on lipid chain saturation," *Phys. Rev. E* **80**, 021931 (2009).
- <sup>40</sup>M. Pöhl, M. F. W. Trollmann, and R. A. Böckmann, "Nonuniversal impact of cholesterol on membranes mobility, curvature sensing and elasticity," *Nat. Commun.* **14**, 8038 (2023).
- <sup>41</sup>F. Sturzenegger, T. Robinson, D. Hess, and P. S. Dittrich, "Membranes under shear stress: Visualization of non-equilibrium domain patterns and domain fusion in a microfluidic device," *Soft Matter* **12**, 5072–5076 (2016).
- <sup>42</sup>M. L. Manning, R. A. Foty, M. S. Steinberg, E.-M. Schoetz, and B. H. Honig, "Coaction of intercellular adhesion and cortical tension specifies tissue surface tension," *Proc. Natl. Acad. Sci. U. S. A.* **107**, 12517–12522 (2010).
- <sup>43</sup>T. Aoki, T. Ohashi, T. Matsumoto, and M. Sato, "The pipette aspiration applied to the local stiffness measurement of soft tissues," *Ann. Biomed. Eng.* **25**, 581–587 (1997).
- <sup>44</sup>Z. Dagan, S. Weinbaum, and R. Pfeffer, "An infinite-series solution for the creeping motion through an orifice of finite length," *J. Fluid Mech.* **115**, 505 (1982).
- <sup>45</sup>N. V. Kosheleva *et al.*, "Cell spheroid fusion: Beyond liquid drops model," *Sci. Rep.* **10**, 12614 (2020).
- <sup>46</sup>I. Pajic-Lijakovic, R. Eftimie, M. Milivojevic, and S. P. A. Bordas, "Multi-scale nature of the tissue surface tension: Theoretical consideration on tissue model systems," *Adv. Colloid Interface Sci.* **315**, 102902 (2023).
- <sup>47</sup>R. A. Foty, G. Forgacs, C. M. Pfleger, and M. S. Steinberg, "Liquid properties of embryonic tissues: Measurement of interfacial tensions," *Phys. Rev. Lett.* **72**, 2298–2301 (1994).
- <sup>48</sup>G. Forgacs, R. A. Foty, Y. Shafrir, and M. S. Steinberg, "Viscoelastic properties of living embryonic tissues: A quantitative study," *Biophys. J.* **74**, 2227–2234 (1998).
- <sup>49</sup>G. Mary *et al.*, "All-in-one rheometry and nonlinear rheology of multicellular aggregates," *Phys. Rev. E* **105**, 054407 (2022).
- <sup>50</sup>M. Urbanska *et al.*, "A comparison of microfluidic methods for high-throughput cell deformability measurements," *Nat. Methods* **17**, 587–593 (2020).